Anisotropy of the mechanical properties of $Li_{1.3}Al_{0.3}Ti_{1.7}(PO_4)_3$ solid electrolyte material

Gang Yan[1*], Shicheng Yu[2], Weiguang Yang[1], Xiaoqiang Li[1], Hermann Tempel[2], Hans Kungl[2], Rüdiger-A. Eichel[2,3,4], Manja Krüger[1], Jürgen Malzbender[1†]

[1] Forschungszentrum Jülich GmbH, Institute of Energy and Climate Research (IEK), Microstructure and Properties of Materials (IEK-2), 52425 Jülich, Germany

[2] Forschungszentrum Jülich GmbH, Institute of Energy and Climate Research (IEK), Fundamental Electrochemistry (IEK-9), 52425 Jülich, Germany

[3] Forschungszentrum Jülich GmbH, Helmholtz-Institute Münster: Ionics in Energy Storage (IEK-12), 48149 Münster, Germany

[4] RWTH Aachen, Institute of Physical Chemistry, 52074 Aachen, Germany

Abstract

Solid state lithium ion batteries have high potential for future energy storage since they promise high energy density and safety, latter being related to the mechanical properties of the materials. For example the micro-battery, being one application of the solid state batteries, requires a thin solid electrolyte, which renders especially anisotropic behavior of the materials' properties important. In particular, $Li_{1+x}Al_xTi_{2-x}(PO_4)_3$ (LATP) is a promising solid electrolyte material that possesses a rhombohedral crystal structure that might lead to such anisotropic mechanical properties. In current work a nanoindentation test is combined with EBSD technique to correlate elastic modulus and hardness of LATP to the crystal orientation. Furthermore, calculations based on the Vlassak-Nix and easy-slip models are adopted to verify the anisotropic mechanical properties. Overall, the experimentally derived elastic modulus and hardness of LATP show

[*] g.yan@fz-juelich.de; tel: +492461616477.; fax: ++492461613699
[†] j.malzbender@fz-juelich.de; tel: +492461616964.; fax: ++492461613699

similar trends. The experimentally derived indentation modulus agrees well with the prediction of the Vlassak-Nix model. The normalization of the experimentally derived hardness and the hardness ratio from the easy-slip model reveal comparable trends. This work aids a deepening of the understanding of the mechanical properties of LATP electrolyte and provides a basis for further improvement of the Vlassak-Nix and easy-slip models in the application to rhombohedral materials.

Keywords: Battery; Solid electrolyte; LATP; anisotropy; elastic modulus; hardness

1. Introduction

Lithium ion batteries gradually substitute traditional batteries, such as lead acid and alkaline batteries, in applications in different areas ranging from micro-devices to spaceships [1]. However, due to their high energy capacity and reduction of safety concerns, recently solid electrolytes are getting more attention in the application of solid state lithium ion batteries, rather than conventional batteries that contain a liquid electrolyte [2, 3]. Nowadays, there are different kinds of solid electrolytes based on glass, solid polymer, amorphous glassy material and inorganic solid electrolytes [4]. In order to enhance micro-power storage in microelectronic devices, potential solid electrolytes need to be selected and optimized for currently evolving stack-up solid state lithium ion batteries, such as polymers and inorganic electrolytes [5]. Currently, the $Li_{1+x}Al_xTi_{2-x}(PO_4)_3$ (LATP) ceramic material is one of the most promising potential inorganic electrolytes, with sodium zirconium phosphate (NASICON) structure that is known to satisfy electro-chemical performance requirements [6].

Although the electro-chemical behavior of solid electrolytes is a main aspect of materials development, the mechanical properties are also an important factor in the practical application. The solid electrolyte suffers from shrinkage and expansion of the electrodes as well as capable lithium penetration during cyclic loading, which implies that the mechanical properties, especially elastic modulus and hardness, should be considered [7, 8]. In addition, the lithium ion battery cell is normally designed into cylindrical, prismatic or pouch types [9], which indicates that the understanding of the mechanical characteristics of the battery materials is necessary to promote the mechanical integrity of the battery cell to endure the structural working mechanical stress and enhance the robustness against to the abusive loading [10]. It has been reported that

the coupled strain rate, ambient condition, anisotropy and the state-of-charge can affect the mechanical behavior of the electrodes and polymer electrolytes [11, 12]. Although mechanical characteristics of solid electrolyte materials have been reported in some works [1, 12-14], reports on LATP's are still limited. Micro-cracking effects on LATP with different grain size were reported by Jackman et al. [15], where it was also indicated that the elastic modulus of the LATP material as obtained via compressive test ranged from 81 to 115 GPa and the fracture toughness measured via single-edge notched beam method was around 1.1 $MPa \cdot m^{1/2}$. The biaxial fracture strength of the LATP material was investigated by Cutler et al. [16], indicating that, with exposure to different solutions, the strength varied from 144 MPa measured in air to 191 MPa measured in mineral oil.

Regarding structural information, Goodenough et al. [17] reported that Al^{3+} can be incorporated into the $LiTi_2(PO_4)_3$ (LTP) structure substituting the place of Ti^{4+}, yielding thereby a higher concentration of Li^+, hence, improving the charging/discharging process. It was reported that LATP possesses a better ionic conductivity at room temperature than both inorganic and organic electrolyte materials [18].

LATP has a rhombohedral crystal structure (space group: $R\bar{3}c$), like LTP [19], of which the unit crystal can be expressed in hexagonal notation [20]. It is known that rhombohedral materials like hematite (α-Fe_2O_3) and corundum (α-Al_2O_3) with space group of $R\bar{3}c$ possess a prominent anisotropy in mechanical properties and also other properties like magnetism [21-23]. Regarding planar micro batteries, where the thickness of the electrolyte can be a few microns (with a total unit cell thickness of < 20 μm) [24], the preferred orientations of the electrolyte ought to be

selected to achieve better separation and support for the electrodes. Thus, the anisotropy of the mechanical properties of LATP needs to be investigated to gain a deeper understanding of the material, which is then also beneficial for any potential application in micro-scale devices.

Often nanoindentation testing is used for characterizing elastic modulus and hardness of materials based on the Oliver & Pharr methodology [25, 26]. Due to the advantages of high accuracy and repeatability, briefness in operation, low requirement of sample preparation etc., this technique has been adopted for plenty of materials using low loads and hence small deformed volume to assess intrinsic properties [27-30]. On the other side, electron backscatter diffraction (EBSD) based on the utilization of scanning electron microscopy (SEM) is commonly applied in characterizing materials regarding information on phase structure, crystal orientation and so on [31]. Hence, in order to study the anisotropic mechanical properties of the LATP, nanoindentation and EBSD analyses are combined to derive correlations of elastic modulus and hardness with lattice rotational angle.

In order to verify results and get deeper insight into underlying mechanisms, two models are used in the current work to predict theoretical elastic modulus and hardness of the LATP material. The Vlassak-Nix model was first proposed in [23] to predict the indentation elastic modulus of anisotropic solids like brass and copper, and later it was applied in the characterization of different materials [32, 33]. On the other side, the easy-slip model was proposed by Csanadi et al. to characterize the anisotropic hardness ratio of materials [34]. Even though this model is not able to predict the exact value of a material's hardness, the variation of

the ratio shows yet the dependence of the hardness on the orientation. Both theories contain several assumptions for the prediction, which will be discussed below.

Hence, the aim of this work is to investigate the anisotropy of the mechanical properties of LATP. The experimentally derived elastic modulus and hardness of LATP are drawn into 3D maps to gain insight into orientation effects, and the results are compared with those data derived via the Vlassak-Nix model and easy-slip model, respectively. Furthermore, the results highlight the advantages of both experimental and predictive approaches to assess the mechanical anisotropy and verify the accuracy of experimental characterization and, at the same time, of assumptions used in the two models. Thus, this work aids an understanding of the mechanical properties of the rhombohedral material LATP and provides a basis for further improvement of the Vlassak-Nix and easy-slip model in the application to rhombohedral materials.

2. Experimental

2.1 Sample preparation

The LATP material was prepared using the same procedures as described in [35, 36]. First, $Ti(OC_3H_8)_4$ and NH_4OH (Aldrich, 30% solution) were mixed in a ratio of 1:2 to obtain a gelatinous precipitate, which was then stored in the deionized water. A $H_2[TiO(C_2O_4)_2]$ solution, available from previous production with addition of 1 M oxalic acid, was mixed with $Al(NO_3)_3$ $9H_2O$ (Aldrich, 99.9%), $(NH_4)_2HPO_4$ (Aldrich, 98%) and 5% excess $LiCOOCH_3$ $2H_2O$ (Aldrich, 98%) and then milled. The uniform solution was heated under stirring up to 80 °C with a hot plate in order to acquire well mixed precipitates. After a pre-annealing of the precursors at 850 °C in air for 5 h, the obtained powders were grinded and then filled into a uniaxial die and

pressed with a load of 40 kN. Afterwards the pressed powders were isostatically compressed with 1425 kN for 10 s and then sintered at 1100 °C for 11 h to obtain the LATP samples.

X-ray diffraction (XRD: Bruker 4 Endeavour) was used to analysis phase and lattice structure of the samples. Here Cu-K_α was employed as XRD radiation source and scanning step were 0.02° / 2 s in the range of 10° to 100°. The porosity of the LATP was measured based on the Archimedes' principle to obtain the relative density of the material, which considers open porosity. Since being a solid electrolyte material, the ionic conductivity of the LATP material was also characterized with a potentiostat (Bio-Logic, SP-300) with the amplitude of 10 mV and frequency ranged in 7 MHz to 1 Hz at room temperature in air. A sample with 0.3 mm thickness and 11.3 mm diameter was tested, where the surface was grinded to obtain a flat surface and eliminate potential effects of surface contamination, and furthermore both contact surfaces were sputtered with gold.

2.2 EBSD of microstructure and orientation

One LATP sample was embedded in water-free resin and then well-polished, with the final step of 0.2 μm SiO_2 abrasive compound mixed with non-water Polyethylene Glycol (PEG), to obtain a smooth surface. It was necessary to use a water-free polishing system to protect the specimen from the loss of lithium via reaction with water, which might affect mechanical properties of the material as well as the correct surface grain orientation information [29]. Scanning electron microscopy (SEM: Zeiss SUPRA 50VP) was adopted to assess the microstructure as well as the indentation marks on the surface of the LATP. The software "AnalySIS pro" was utilized to analyze the microstructure of the LATP material in order to calculate the grain size. Electron backscatter diffraction (EBSD) integrated within the SEM was

employed to characterized the orientation of the grains of the LATP sample. The EBSD image with high resolution was taken with an accelerating voltage of 15 kV, specimen tilt degree of 70 ° and acquisition speed of 39.5 Hz.

The orientation of the LATP grains was analyzed on the basis of the measured EBSD results with the open source toolbox MTEX, which can be run in Matlab for evaluating the crystallographic texture [37]. In the EBSD analysis the Euler angles ($\varphi 1$, Φ, $\varphi 2$) are used to describe the grain orientation. The illustration of relation between the crystal coordinate system and principal sample coordinate system represented by Euler angles can be found in Fig. S1.

Since the LATP material is a rhombohedral mineral with structure like corundum, only the angle Φ and $\varphi 2$ were considered as the relevant index to see the possible effect of orientation on the elastic modulus and hardness in this study. The three angles are theoretically in range of [0, 2π]. As the corundum structure of the LATP material can be computed into a hexagonal lattice [38], considering the properties of the hexagonal symmetry, the angle Φ is in the range of [0, $\pi/2$] and the angle $\varphi 2$ in the range of [0, $\pi/3$]. Note that, the Euler angles were recalculated to characterize the angle between the random plane and basal plane, prismatic planes. In this work, the angle Φ represents the angle from parallel of basal (0001) orientation plane to vertical of basal plane, and the angle $\varphi 2$ represents the angle between two prismatic $(10\bar{1}0)$ type planes during which rotating through one prismatic $(11\bar{2}0)$ type plane.

2.3 Nanoindentation

The nanoindentation test, which is a frequently used method in assessment of the mechanical behavior of materials [39, 40], was carried out to characterize the anisotropic mechanical properties of the LATP material. A NanoTest Xtreme test setup from Micro Materials® was utilized in the current work with a diamond Berkovich tip. The indentation tests were conducted at room temperature in a depth control mode and fused silica was used as a standard material to calibrate tip and machine compliance to ensure the data validity [41, 42]. A depth control mode was chosen instead of a load control mode to avoid localized large damage of the specimen due to large imprints, since imprints close to pores can be very large and interacted with neighboring indentations. The holding time at maximum load of 300 nm and rate of acquisition during the indentations were 10 s and 20 Hz, respectively.

As indicated above, the values of E and H were derived from the load-displacement data via the Oliver-Pharr methodology [26]. To obtain the elastic modulus of the LATP material, a Poisson's ratio, ν_i = 0.07, and Young's modulus, E_i = 1141 GPa, of the diamond indenter tip were adopted and a Poisson's ratio of ν_s = 0.25 was used for the LATP material [15, 43].

The indentation tests were carried out on a surface area which was first characterized by EBSD. Due to the test limitation of the machine (maximum 400 impressions per test set), two individual areas were chosen to conduct the indentation mapping. The distance between the imprints was fixed to 5 μm in order to avoid interaction of the stress field of neighboring impressions. When establishing the dependence of indentation results on grain orientation, only indents which were inside LATP gains were taken into consideration. Indentations which were

close to a grain boundary or located within a distance of 5 μm to pores were ignored to rule out effects that might lead to additional complexities in the correlation of mechanical data.

2.4 Prediction of elastic modulus and hardness

In order to investigate non-experimentally potential anisotropies in the mechanical properties of LATP, two theoretical models are adopted as a basis for later comparison with experimental results. These models permit prediction of modulus and hardness, respectively. The Vlassak-Nix model [23, 44] is used here to calculate the anisotropic elastic modulus related to the elastic constants of LATP single crystal, since this model has been successfully applied in predicting the elastic modulus of sapphire material, especially for the basal plane as well as in other the two planes. Results matched with those reported in [45]. The 'easy-slip' model [34] is adopted to simulate the anisotropic hardness variation of LATP material related to the slip system. It was first introduced by the Csanadi et al. to calculate the hardness - orientation dependency of WC material and the analytical calculated results fitted very well with experimental results in [46].

The Vlassak-Nix model assumes that a rigid tip penetrates into an anisotropic elastic plane of a solid [23, 44]. In this model the Green's function for calculating the vertical displacement of the surface at a point load is adopted. A Rayleigh-Ritz approximation is applied to establish a force function which can form an elliptical contact area based on Green's function, with the assumption that the Laplacian operator in two-dimension of the surface is positive for the maximum displacement in the contact area and negative for the maximum displacement in the unloaded area.

Another assumption is that a conical rigid indenter was introduced to maintain the same orientation and eccentricity of the contact zone for varying displacement. In order to simplify the model further, the contact area is set into a circular area, which leads to the calculation of the indentation modulus M as shown in equation (1). The h_0 here is the first item in the Fourier series representation of function $h(\theta)$ related to θ, which is demonstrated in equation (2). Here θ is the angle represented direction variation of point load in a specific surface ranged in $[0, \pi]$. The α_i is the direction cosines of the angle between the load direction and the crystal coordinate system axes. Equation (3) and equation (4) are the expansion form in equation (2) and equation (3), respectively. In equation (3) one right-hand Cartesian coordinate ($\bar{m}$, $\bar{n}$, t) is built where the t axis was vertical to the load direction, in which φ is the angle between the vector $\bar{m}$ and one fixed vector in the ($\bar{m}$, $\bar{n}$) plane. The C_{ijkm} in equation (4) contains the elastic parameters of the anisotropic material based on the elastic constants of the material. The transition of the parameter C_{ijkm} from the elastic constants C_{pq} follows the regulation: the tensors ij (or km) reflected to the tensor p (or q) with the relation of 11 → 1, 22 → 2, 33 → 3, 23 and 32 → 4, 13 and 31 → 5, 21 and 12 → 6.

$$M = \frac{1}{\pi h_0} \tag{1}$$

$$(\theta) = \frac{1}{8\pi^2}(\alpha_k B_{km}^{-1} \alpha_m) \tag{2}$$

$$B_{js}(\mathbf{t}) = B_{sj}(\boldsymbol{t}) = \frac{1}{8\pi^2}\int_0^{2\pi}\left\{(\mathbf{mm})_{js} \quad (\mathbf{mn})_{jk}(\mathbf{nn})_{kr}{}^{-1}(\mathbf{nm})_{rs}\right\} d\varphi \tag{3}$$

$$(\mathbf{ab})_{jk} = a_i C_{ijkm} b_m \tag{4}$$

$$C_{pq} = \begin{matrix} 226.0 & 86.7 & 43.9 & 7.9 & 0.0 & 0.0 \\ 86.7 & 226.0 & 43.9 & 7.9 & 0.0 & 0.0 \\ 43.9 & 43.9 & 116.3 & 0.0 & 0.0 & 0.0 \\ 7.9 & 7.9 & 0.0 & 48.6 & 0.0 & 0.0 \\ 0.0 & 0.0 & 0.0 & 0.0 & 48.6 & 7.9 \\ 0.0 & 0.0 & 0.0 & 0.0 & 7.9 & 49.6 \end{matrix} \quad (5)$$

By now, no elastic constants results have been reported for the $Li_{1+x}Al_xTi_{2-x}(PO_4)_3$ material. The structure of $Li_{1+x}Al_xTi_{2-x}(PO_4)_3$ material is the same as that of $LiTi_2(PO_4)_3$ and the substitution of Al^{3+} into the lattice structure yields no obvious contribution to the lattice parameter, as shown in Table 1, compared with that of $a^*=b^*=0.8535$ nm, $c^*=2.0883$ nm as reported in [19]. Hence, the elastic constants of $LiTi_2(PO_4)_3$ with the unit GPa as given in equation (5), which were calculated via ab initio method by Deng et al. [43], were employed in the Vlassak-Nix model. Taking the symmetry of hexagonal structure into consideration, as illustrated in Fig. S1, in the Vlassak-Nix model, the angle Φ from basal plane to the perpendicular direction with 1° per step, and some specific angles of $\varphi 2$ in the basal plane, were adopted to calculate the orientation dependency of the indentation modulus.

The "easy-slip" model, on the other side, which has been adopted here to predict the hardness variation related to the orientation of the anisotropic material, is based on one principal hypothesis that the stress distribution is confined in the indentation area which is uniformed, i.e., the stress component surrounding the indenter is compressive and vertical to the indenter profile [34, 46]. This model contains several assumptions and a schematic is shown in Fig. S2. The hardness can be calculated as expressed in equation (6). First is that the conical rigid indenter with a semi-angle γ of 65° is introduced into the model to simplify the calculation and also reaches a consensus with the Vlassak-Nix model. Additionally, friction during indentation is not

considered. The second assumption is that just one dislocation slip is considered as the plastic deformation fraction is small. The slip can only occur when the shear stress reaches a critical value for a specific direction, which results in the name of "easy-slip". Here the Schmid factor for calculating the normal stress, as illustrated in Fig. S2 (b), is introduced in equation (7), assuming that the critical resolved shear stress is a constant, and the calculation of normal stress follows equation (8).

The third assumption is about the slip systems of the LATP material, which is different in this work compared to that of WC reported in the Csanadi et al.'s work [34]. To the best of our knowledge, no investigations have been reported on the slip systems of the LATP or LTP materials. For the materials with R $\bar{3}$ c crystal system like LATP, two kinds of crystal deformations can occur simultaneously, which are slipping and twinning [47, 48]. It has been confirmed that for the rhombohedral crystal structure with computed hexagonal lattice parameter ratio of $c^*/a^* > 1.633$, the slide systems are {0001} <11$\bar{2}$0> in basal plane and {11$\bar{2}$0} <1$\bar{1}$00> in prismatic planes, whereas the slip in pyramidal plane is out of consideration, since this type of slip can be unidirectional [38, 49].

Thus, in total 6 slip systems are considered in the easy slip model with $\overline{n_\iota}$ as the normal vector for the slip plane and $\overline{v_{ij}}$ as the slip direction vector as illustrated in Fig. S2 (c): $\overline{n_0}$ = (0001): $\overline{v_{01}}$ = [11$\bar{\bar{2}}$0], $\overline{v_{02}}$ = [2$\bar{1}\bar{1}$0], $\overline{v_{03}}$ = [$\bar{1}$2$\bar{1}$0], $\overline{n_1}$== (11$\bar{2}$0): $\overline{v_{11}}$ = [1$\bar{1}$00], $\overline{n_2}$ = ($\bar{1}$2$\bar{1}$0): $\overline{v_{21}}$ = [10$\bar{1}$0], $\overline{n_3}$ = (2$\bar{1}\bar{1}$0): $\overline{v_{31}}$ = [01$\bar{1}$0]. The vectors $\overline{n_\iota}$ and $\overline{v_{ij}}$ should be normalized during calculation. An improvement of the original model is made according to [46], i.e. that the average of the maximum Schmid factor by the surrounding of indenter at the specific rotation angle Φ is

considered rather than the maximum Schmid factor directly as shown in equation (9). With these entire mentioned hypotheses', the relation between hardness and the orientation of the LATP material can be expressed as a ratio of hardness at specific plane to hardness at prismatic plane as demonstrated in equation (10), which is equal to the inverse ratio of the corresponding average maximum Schmid factor.

$$H = \frac{F}{A} = \frac{\sigma \times A_C}{A} \tag{6}$$

$$\tau = \frac{dF \times cos\alpha}{dA'} = \frac{dF \times cos\alpha}{\frac{dA}{cos\beta}} = \frac{dF}{dA} \times cos\alpha \times cos\beta = \sigma \times cos\alpha \times cos\beta = \sigma \times m(\varphi) \tag{7}$$

$$\sigma = \left(\frac{\tau}{m(\varphi)}\right)_{min} = \frac{\tau_{CRSS}}{(m(\varphi))_{avg.max,\,\varphi}} \tag{8}$$

$$m(\varphi)_{avg.max,\varphi}(\Phi) = \frac{1}{2\pi}\int_0^{2\pi} max_{i,j}\left(m_{i,j}(\Phi,\varphi)\right) d\varphi \tag{9}$$

$$\frac{H(\Phi)}{H_{prismatic}} = \frac{H(\Phi)}{H(\Phi{=}90°)} = \frac{m_{avg.max,\varphi}(\Phi{=}90°,\varphi)}{m_{avg.max,\varphi}(\Phi,\varphi)} \tag{10}$$

3. Results and Discussion

3.1 Composition, conductivity and orientational distribution

One as-sintered LATP sample was characterized with XRD to analyze the phase structure. The resulting XRD pattern in Fig. 1 reveals that the peaks can be fitted well with the reference pattern $Li_{1.2}Al_{0.2}Ti_{1.8}(PO_4)_3$ (rhombohedral crystal structure, $R\bar{3}c$). A small amount of secondary phase of $AlPO_4$ (Orthorhombic crystal structure, $C222_1$) can be observed in the material, which can be attributed to the Li loss during sintering. As the sintering process was conducted at high

temperature Li evaporated, which appeared to result in an Al^{3+} amount above the solubility limitation, and then secondary phase formation [50].

Elastic modulus and hardness of $AlPO_4$ are around 77 GPa [51, 52] and 3.5 - 5.5 GPa [53], respectively, which means that they are significantly lower than the mechanical parameters of the LATP characterized here, hence any effect of localized testing of this phase would have been obvious. Hence, overall, the effect of the secondary phase on the experimental results can be neglected since the amount of $AlPO_4$ is low and $AlPO_4$ is located in the grain boundaries, and during the analysis within a grain only the indentations which yielded similar load-displacement curves were chosen to do the mechanical properties evaluation corresponding to the specific grain orientation.

The lattice parameters of LATP calculated from the Rietveld refinement, as shown in Table 1, are in good agreement with that of $a^*=b^*$=0.84941 - 0.85068 nm, c^*=2.08586 - 2.09085 nm as reported in [54]. Since the LATP crystal structure is the same as that of $LiTi_2(PO_4)_3$, and even with Al^{3+} doping the lattice parameter is similar as that of $LiTi_2(PO_4)_3$ ($a^*=b^*$=0.8535 nm, c^*=2.0883 nm) [19], the elastic constants of $LiTi_2(PO_4)_3$ and the lattice parameters shown in Table 1 are used for the Vlassak-Nix model below.

The microstructural images at different magnifications of the LATP sample can be seen in Fig. S3. From Fig. S3 (a) the pores are found homogeneously distributed in LATP. The microstructure at a higher magnification is shown in Fig. 3 (b), from which the grain size of LATP has been derived via the software “AnalySIS pro” as 12.1 ± 5.9 μm. The pores are located

both in grain boundaries and inside grains, where the former are irregular and the latter are rather round. The spherical pores inside the grains can be ascribed to the hydrostatic pressure of air, which was preserved in the grown grains during pre-annealing [55]. The Archimedes' method was used here to characterize the porosity of the LATP, hence open pores did not enter the porosity calculation. The relative density of the LATP sample calculated by the ratio of bulk density to theoretical density of 2.947 g/cm^3 [15] is 96.7%. It is well known that the porosity can decrease the mechanical properties of a material like elastic modulus and hardness [56, 57]. However, in this work the indentation test was conducted in a small local region of single grains so that effects of pores on the obtained properties can be ignored. Furthermore, as shown in Fig. S3 (b), the grain boundaries are very distinct, which is helpful in localizing the corresponding indentations in the EBSD mapping and eliminating these data.

Being a solid electrolyte material, as a basic characteristic of LATP, the electro-chemical behavior has to be investigated. The ionic conductivity of a LATP pellet was measured with a potentiostat at room temperature (~ 25 °C). In Fig. 2 the Nyquist plots of the imaginary against real impedance of the LATP sample (0.3 mm thickness) is shown, of which the intercept at high frequency was used as representative for the conductivity of the sample. The derived conductivity of LATP in this work is 0.18 mS/cm, which agrees well with the results of 0.2 mS/cm reported in [15, 58].

The chosen areas for indentation are shown in Fig. 3 (a). The red and blue frames with the corresponding EBSD results in all three axes are displayed in Fig. 3 (b). Only imprints were considered in the analysis of the data that possessed a regular shape and were located not too

close to pores and grain boundaries. The indentations are grouped by the grains with different orientations and then elastic modulus and hardness are analyzed. For analyzation the certain grains with at least 3 indents are then considered.

Fig. 3 (b) shows that the EBSD images for the well-polished LATP are quite clear, which verifies that any potentially affected layer on the surface was removed, since it was reported that the EBSD pattern quality correlated adversely with the defect density [59]. Thus the mechanical properties of LATP can be analyzed without consideration of potential residual stress effects. Furthermore, the EBSD results indicate that the LATP grains are orientated highly randomly, which permits an appropriate investigation of the anisotropic mechanical properties.

3.2 Mechanical properties

Typical indentation load-depth curves for three specific planes are shown in Fig. 4, in which (a) shows the curve for an imprint on the basal plane; (b) and (c) show curves for the prismatic type $(10\bar{1}0)$ and $(11\bar{2}0)$ planes. The specific plane was determined based on the Euler angle Φ, i.e. the angle between the selected plane and the basal plane or prismatic plane, which was supposed to be less than 10°. Since the indentation test was carried out in a depth control mode, all three curves reached a depth of 300 nm, however, since the holding time at maximum load was 10 s (to avoid reversible plasticity) the maximum depth before unloading was slightly larger than 300 nm.

The curve shapes, which are the basis for obtaining the experimental elastic modulus and hardness, for all three planes are different, which verified that the LATP material's mechanical

properties are anisotropic. Obviously the maximum loads for the two prismatic planes are very similar, whereas the maximum load for the basal plane was much higher. As illustrated in Fig. 3, some of the indentations were out of the area characterized by the EBSD pattern and some are close to the defects like pores, which needed to be eliminated from the analysis. Thus, the amount of the valid data that could be associated with different grains was limited.

Elastic modulus and hardness of the LATP sample are presented in three dimensional charts with the two axes representing the angle from the basal orientation (Φ) and the angle from prismatic orientation ($\varphi 2$), as can be seen in Fig. 5. The data was expanded via the software "Origin" converting the worksheet to matrix to make the 3D colorful surface map. Here the surface mapping has no physical meaning and is only used as a guide for eyes to observe clearly the dependency of mechanical properties on rotation angles. To permit a clearer understanding of the graphs the deviations of E and H are shown and discussed in more detail below.

It can be seen in Fig. 5 that elastic modulus and hardness of LATP reveal a similar trend with variation of the angles (Φ, $\varphi 2$). It is notable that, with the increasing of Φ, i.e., angle of the indented plane rotating from the basal plane towards the prismatic plane, E and H decrease significantly. Yet the $\varphi 2$, i.e., angle of the indented plane rotated from prismatic $(10\bar{1}0)$ type plane to another $(10\bar{1}0)$ plane through the prismatic $(11\bar{2}0)$ type plane, has no obvious effect on the mechanical properties. This manifests that the rotation angle Φ is the dominant factor influencing the anisotropic behavior of the LATP material, which agrees well with the hexagonal material β-Si_3N_4, as reported in [46].

The elastic modulus decreases from 150 ± 3 GPa for the basal plane to 107 ± 4 GPa for the prismatic plane, whereas the hardness decreases from 10.0 ± 0.2 GPa for the basal plane to 5.5 ± 0.3 GPa for the prismatic plane, each being the individual maximum and minimum experimental data points regarding to the individual grains. It was reported by Jackman et al. that *E* of LATP ranged from 81 to 115 GPa and *H* was 7.1 ± 0.4 GPa [15], and Deng et al. reported that *E* of the $LiTi_2(PO_4)_3$ type material ranged from 139.0 to 152.5 GPa as derived via first principle calculation [43]. Taking orientation effects into consideration, elastic modulus and hardness obtained here are in good agreement with these data.

Typical morphologies of imprints in different magnifications can be seen in Fig. 6 (a) and (b). It can be found that the indentations are homogeneously distributed over the sample surface in Fig. 6 (a). The distance between the indents was 5 μm and no interaction between the imprints inside the grain is visible in Fig. 6 (b), which manifests that the indentation results represent the local property within each selected grain. With the aid of the green triangle it can be seen that the models assuming sink-in behavior is adequate. In addition, around the indentations no clear slip lines can be observed.

3.3 Calculation results

As outlined above, the Vlassak-Nix and easy-slip models are adopted here to calculate indentation elastic modulus and hardness ratio, respectively, corresponding to the rotation angle of the crystal structure, as shown in Fig. 7. The indentation modulus and hardness are derived as a function of Φ from 0° to 180° with 1° per step to show a detailed symmetric variation. In order to see any effects in the mechanical properties with respect to angle $\varphi 2$, i.e., the initio angle for

calculation between the normal of the indented surface and the *X*-*Z* plane of the crystal coordinate system at *X*-*Y* plane, three typical plots, at $\varphi 2$ = -30°, 0° and 30°, are selected for both indentation modulus and hardness ratio.

It can be seen that in the interval of Φ from 0° to 90°, i.e. the indented plane being rotated from the basal plane to the prismatic plane, the indentation modulus decreases continuously with a maximum value of 177 GPa at 0° and a minimum value of 118 GPa at 90°. With respect to the hardness ratio, results for the hardness at 90° are used as a reference value; the ratio is highest of 2.0 at 0° and then decreases to 0.96 at 70°, afterwards the value rises to 1 at 90° in a semi-period.

The angle $\varphi 2$ has only a small effect on the indentation modulus, i.e. with increase of $\varphi 2$ the indentation modulus and hardness plots shift right with the same maximum and minimum value, whereas the $\varphi 2$ angle has no observable influence on the hardness ratio. Thus it can be confirmed that the angle Φ is the dominant factor in affecting the anisotropic mechanical properties of rhombohedral LATP material, and, therefore, the comparison of the experimental results and calculated results is discussed only in terms of the Φ angle.

3.4 Comparison of experimental and calculated results

In order to compare both the experimental and the Vlassak-Nix model's indentation modulus, the value based on the equation $M = \frac{E}{1-\vartheta_s{}^2}$ was used. So to permit a comparison of the experimental results and the two model's predictions, the experimental and model's results of elastic modulus and hardness are plotted as a function of angle Φ in Fig. 8, where the experimental hardness is normalized (using the value at Φ = 90° as reference data).

It can be seen from Fig. 8 (a) that the experimental normalized E possesses the same trend as the one predicted by the Vlassak-Nix model. Nevertheless, the indentation modulus values, especially at low Φ angles, are slightly lower than the data derived from the theoretical model. In the current work the calculated experimental indentation modulus decreases from 160 ± 4 GPa for the basal plane to 114 ± 4 GPa for the prismatic plane. It can be observed that the extreme value of the experimentally obtained indentation modulus is slightly lower than the one predicted from the Vlassak-Nix model, i.e. the difference is 10%. The normalized hardness shows a decreasing trend with increasing angle, similar to that of the data derived from the easy-slip model, as shown in Fig. 8 (b). The ratio of the maximum of the experimental data is around 1.8, being lower than that of 2.0 from the easy-slip model. The experimental normalized H for Φ values in the range of 20° - 70° is higher than the predicted data as well as the reference data point, while the easy-slip model yields a minimum value at Φ of 70°. No difference can be obtained for the experimentally derived and predicted hardness value, since due to the limitation of the easy-slip model no absolute value of hardness can be calculated and only the variation trend can be anticipated.

The differences between the experimental and theoretical outcomes can be a result of many factors. Due to the randomness of the grain orientation, some experimental points especially the data at Φ of 0° were missing. In addition, the usage of the elastic constants based on $LiTi_2(PO_4)_3$ material and the 6 slip systems simplified via ruling out the unidirectional slip lowered down the accuracy of the prediction of the two models. Even so, the insufficient Vlassak-Nix model and easy-slip model still permit a close estimate of the elastic modulus and hardness of the LATP

material although further improvement appears to be possible in future works concentrating on these predictive approaches. In solid-state lithium batteries with thick electrolyte the average mechanical properties of the electrolyte are considered, whereas for the micro-batteries the thickness of the electrolyte goes down to the grain size, the mechanical properties of individual grains like elastic modulus and hardness become prominent effects and need to be taken into account of battery design and promotion.

4. Conclusions

The anisotropy of the mechanical properties of a solid electrolyte material was investigated in this work via indentation mapping test with depth control mode at room temperature and associate EBSD characterization. The LATP ceramic electrolyte with a rhombohedral crystal structure was studied and the imprints after indentation were analyzed. The experimental elastic modulus and hardness as a function of rotation angle from basal plane to prismatic plane were assessed and compared with those predicted by the Vlassak-Nix and easy-slip model, respectively, which were used to calculate a theoretical modulus and hardness ratio, respectively.

Noticeable anisotropic mechanical properties of LATP material were observed. The experimental elastic modulus and hardness of LATP showed a similar trend, i.e. that the rotation angle $\varphi 2$ between two prismatic $(10\bar{1}0)$ type planes had no detectable influence, whereas when the rotation angle Φ from basal plane to prismatic plane increased, E and H value decrease conspicuously. The Vlassak-Nix and easy-slip model demonstrated that the angle $\varphi 2$ has a negligible effect and the difference between the results of the two models' results was that, as the

angle Φ increased, the indentation modulus from the Vlassak-Nix model decreased continuously while the hardness ratio derived by the easy-slip model decreased to the minimum value at 70° and then increased slightly. The comparison of experimental results and theoretical calculation was discussed only in terms of the rotation angle Φ, since the angle Φ appears to be the dominant factor on the mechanical properties of LATP.

The experimental indentation modulus fitted well with the prediction of the Vlassak-Nix model, yet the model showed an around 10% higher extremum (118 - 177 GPa) than the experimental results (114 - 160 GPa). The experimental hardness was normalized to compare with the hardness ratio from the easy-slip model and the trend of two results was comparable. The difference between the experimental results and the models' results can be ascribed to simplification for calculation such as that the Vlassak-Nix model adopted the $LiTi_2(PO_4)_3$ material's elastic constants, the easy-slip model took the simplified 6 slip systems into account. Besides, more experimental data points could be gained in future work, especially the result around Φ = 0°. This work presents data supporting an understanding of the anisotropic mechanical properties of the rhombohedral crystalline LATP material and provides a basis for further improvement of the Vlassak-Nix and easy-slip model.

Acknowledgements

The authors would like to thank Dr. E. Wessel, Dr. D. Grüner and Mr. M. Ziegner for the supporting the work with SEM, EBSD and XRD investigation. Support from Prof. Dr. Lorenz Singheiser is highly acknowledged. Gang Yan gratefully acknowledges the support from the China Scholarship Council (CSC) of China.

Appendix A. Supplementary information

The supplementary information accompanying the manuscript is: i) illustration of the Euler angles; ii) schematic of the assumptions in “easy-slip” model; iii) surface observation of LATP sample.

References

[1] Tarascon J-M, Armand M. Issues and challenges facing rechargeable lithium batteries. Nature. 2001;414:359-67.
[2] Armand M, Tarascon J-M. Building better batteries. Nature. 2008;451:652-7.
[3] Scrosati B, Garche J. Lithium batteries: Status, prospects and future. J Power Sources. 2010;195:2419-30.
[4] Besenhard JO. Handbook of battery materials: John Wiley & Sons; 2008.
[5] Oudenhoven JF, Baggetto L, Notten PHJAEM. All‐solid‐state lithium‐ion microbatteries: a review of various three‐dimensional concepts. 2011;1:10-33.
[6] Wu H, Chan G, Choi JW, Ryu I, Yao Y, McDowell MT, et al. Stable cycling of double-walled silicon nanotube battery anodes through solid–electrolyte interphase control. Nature nanotechnology. 2012;7:310.
[7] Balakrishnan P, Ramesh R, Kumar TP. Safety mechanisms in lithium-ion batteries. J Power Sources. 2006;155:401-14.
[8] Monroe C, Newman J. The impact of elastic deformation on deposition kinetics at lithium/polymer interfaces. J Electrochem Soc. 2005;152:A396-A404.
[9] Horiba T. Lithium-ion battery systems. Proceedings of the IEEE. 2014;102:939-50.
[10] Liu B, Jia Y, Yuan C, Wang L, Gao X, Yin S, et al. Safety Issues and Mechanisms of Lithium-ion Battery Cell Upon Mechanical Abusive Loading: A Review. Energy Storage Materials. 2019.
[11] Wang L, Yin S, Zhang C, Huan Y, Xu J. Mechanical characterization and modeling for anodes and cathodes in lithium-ion batteries. J Power Sources. 2018;392:265-73.
[12] Xu J, Wang L, Guan J, Yin S. Coupled effect of strain rate and solvent on dynamic mechanical behaviors of separators in lithium ion batteries. Materials & Design. 2016;95:319-28.
[13] Hu X, Cheng X, Qin S, Yan G, Malzbender J, Qiang W, et al. Mechanical and electrochemical properties of cubic and tetragonal Li x La 0.557 TiO 3 perovskite oxide electrolytes. Ceram Int. 2017.
[14] Yan G, Nonemacher JF, Zheng H, Finsterbusch M, Malzbender J, Krüger M. An investigation on strength distribution, subcritical crack growth and lifetime of the lithium-ion conductor Li 7 La 3 Zr 2 O 12. Journal of Materials Science.1-11.
[15] Jackman SD, Cutler RA. Effect of microcracking on ionic conductivity in LATP. J Power Sources. 2012;218:65-72.
[16] Jackman SD, Cutler RA. Stability of NaSICON-type Li1. 3Al0. 3Ti1. 7P3O12 in aqueous solutions. J Power Sources. 2013;230:251-60.
[17] Goodenough J, Hong H-P, Kafalas J. Fast Na+-ion transport in skeleton structures. Materials Research Bulletin. 1976;11:203-20.
[18] Fergus JW. Ceramic and polymeric solid electrolytes for lithium-ion batteries. J Power Sources. 2010;195:4554-69.
[19] LiTi2(PO4)3 (LiTi2[PO4]3) Crystal Structure: Datasheet from "PAULING FILE Multinaries Edition – 2012" in SpringerMaterials (https://materials.springer.com/isp/crystallographic/docs/sd_0543087). In: Villars P, Cenzual K, editors.: Springer-Verlag Berlin Heidelberg & Material Phases Data System (MPDS), Switzerland & National Institute for Materials Science (NIMS), Japan.
[20] Snow J, Heuer A. Slip systems in Al2O3. J Am Ceram Soc. 1973;56:153-7.
[21] Stevenson ME, Kaji M, Bradt RC. Microhardness anisotropy and the indentation size effect on the basal plane of single crystal hematite. J Eur Ceram Soc. 2002;22:1137-48.
[22] Uyeda S, Fuller M, Belshe J, Girdler R. Anisotropy of magnetic susceptibility of rocks and minerals. Journal of Geophysical Research. 1963;68:279-91.
[23] Vlassak JJ, Nix W. Measuring the elastic properties of anisotropic materials by means of indentation experiments. Journal of the Mechanics and Physics of Solids. 1994;42:1223-45.

[24] Wang Y, Liu B, Li Q, Cartmell S, Ferrara S, Deng ZD, et al. Lithium and lithium ion batteries for applications in microelectronic devices: A review. J Power Sources. 2015;286:330-45.
[25] Pharr G, Oliver W. Measurement of thin film mechanical properties using nanoindentation. Mrs Bull. 1992;17:28-33.
[26] Oliver WC, Pharr GM. An Improved Technique for Determining Hardness and Elastic-Modulus Using Load and Displacement Sensing Indentation Experiments. J Mater Res. 1992;7:1564-83.
[27] Malzbender J, de With G. The use of the indentation loading curve to detect fracture of coatings. Surface and Coatings Technology. 2001;137:72-6.
[28] Malzbender J, de With G. The use of the loading curve to assess soft coatings. Surface and Coatings Technology. 2000;127:265-72.
[29] Wang A-N, Nonemacher JF, Yan G, Finsterbusch M, Malzbender J, Krüger M. Mechanical properties of the solid electrolyte Al-substituted Li7La3Zr2O12 (LLZO) by utilizing micro-pillar indentation splitting test. J Eur Ceram Soc. 2018.
[30] Nonemacher JF, Hüter C, Zheng H, Malzbender J, Krüger M, Spatschek R, et al. Microstructure and properties investigation of garnet structured Li 7 La 3 Zr 2 O 12 as electrolyte for all-solid-state batteries. Solid State Ionics. 2018;321:126-34.
[31] Malzbender J, Steinbrech R, Singheiser L. A review of advanced techniques for characterising SOFC behaviour. Fuel Cells. 2009;9:785-93.
[32] Csanádi T, Németh D, Zhang C, Dusza J. Nanoindentation derived elastic constants of carbon fibres and their nanostructural based predictions. Carbon. 2017;119:314-25.
[33] Hu Y, Zhao X, Vlassak JJ, Suo Z. Using indentation to characterize the poroelasticity of gels. Appl Phys Lett. 2010;96:121904.
[34] Csanádi T, Bl'anda M, Chinh NQ, Hvizdoš P, Dusza J. Orientation-dependent hardness and nanoindentation-induced deformation mechanisms of WC crystals. Acta Mater. 2015;83:397-407.
[35] Yu S, Mertens A, Gao X, Gunduz DC, Schierholz R, Benning S, et al. Influence of microstructure and AlPO4 secondary-phase on the ionic conductivity of Li 1. 3 Al 0. 3 Ti 1. 7 (PO 4) 3 solid-state electrolyte. Functional Materials Letters. 2016;9:1650066.
[36] Yan G, Yu S, Nonemacher JF, Tempel H, Kungl H, Malzbender J, et al. Influence of sintering temperature on conductivity and mechanical behavior of the solid electrolyte LATP. Ceram Int. 2019.
[37] Mainprice D, Hielscher R, Schaeben H. Calculating anisotropic physical properties from texture data using the MTEX open-source package. Geological Society, London, Special Publications. 2011;360:175-92.
[38] Clayton J. Modeling finite deformations in trigonal ceramic crystals with lattice defects. International Journal of Plasticity. 2010;26:1357-86.
[39] Hu X, Cheng X, Qin S, Yan G, Malzbender J, Qiang W, et al. Mechanical and electrochemical properties of cubic and tetragonal LixLa0. 557TiO3 perovskite oxide electrolytes. Ceram Int. 2018;44:1902-8.
[40] Huang B, Malzbender J, Steinbrech R, Wessel E, Penkalla H, Singheiser L. Mechanical aspects of ferro-elastic behavior and phase composition of La0. 58Sr0. 4Co0. 2Fe0. 8O3 δ. J Membrane Sci. 2010;349:183-8.
[41] Vachhani S, Doherty R, Kalidindi S. Effect of the continuous stiffness measurement on the mechanical properties extracted using spherical nanoindentation. Acta Mater. 2013;61:3744-51.
[42] Siu K, Ngan A. The continuous stiffness measurement technique in nanoindentation intrinsically modifies the strength of the sample. Philos Mag. 2013;93:449-67.
[43] Deng Z, Wang Z, Chu I-H, Luo J, Ong SP. Elastic properties of alkali superionic conductor electrolytes from first principles calculations. J Electrochem Soc. 2016;163:A67-A74.
[44] Vlassak J, Ciavarella M, Barber J, Wang X. The indentation modulus of elastically anisotropic materials for indenters of arbitrary shape. Journal of the Mechanics and Physics of Solids. 2003;51:1701-21.

[45] Wachtman Jr J, Tefft W, Lam Jr D, Stinchfield R. Elastic Constants of Synthetic Single‐Crystal Corundum at Room Temperature. J Am Ceram Soc. 1960;43:334-.
[46] Csanádi T, Németh D, Dusza J, Lenčéš Z, Šajgalík P. Nanoindentation induced deformation anisotropy in β-Si3N4 ceramic crystals. J Eur Ceram Soc. 2016;36:3059-66.
[47] Kronberg M. Plastic deformation of single crystals of sapphire: basal slip and twinning. Acta Metallurgica. 1957;5:507-24.
[48] Nowak R, Sekino T, Maruno S, Niihara K. Deformation of sapphire induced by a spherical indentation on the (1010) plane. Appl Phys Lett. 1996;68:1063-5.
[49] Siemes H, Klingenberg B, Rybacki E, Naumann M, Schäfer W, Jansen E, et al. Glide systems of hematite single crystals in deformation experiments. Ore Geol Rev. 2008;33:255-79.
[50] Kali R, Mukhopadhyay A. Spark plasma sintered/synthesized dense and nanostructured materials for solid-state Li-ion batteries: Overview and perspective. J Power Sources. 2014;247:920-31.
[51] Shpakov V, Tse J, Belosludov V, Belosludov R. Elastic moduli and instability in molecular crystals. Journal of Physics: Condensed Matter. 1997;9:5853.
[52] Zhou Y, Liu B. Theoretical investigation of mechanical and thermal properties of MPO4 (M= Al, Ga). J Eur Ceram Soc. 2013;33:2817-21.
[53] HIROTA K, BRADT RC. THE MICROHARDNESS INDENTATION SIZE/LOAD EFFECT (ISE) IN SINGLE-CRYSTAL, BERLINITE. Advanced Materials' 93, I: Elsevier; 1994. p. 441-4.
[54] Pérez-Estébanez M, Isasi-Marín J, Többens D, Rivera-Calzada A, León C. A systematic study of Nasicon-type Li1+ xMxTi2 x (PO4) 3 (M: Cr, Al, Fe) by neutron diffraction and impedance spectroscopy. Solid State Ionics. 2014;266:1-8.
[55] Yang J-F, Zhang G-J, Ohji T. Porosity and microstructure control of porous ceramics by partial hot pressing. J Mater Res. 2001;16:1916-8.
[56] Silva RO, Malzbender J, Schulze-Küppers F, Baumann S, Guillon O. Mechanical properties and lifetime predictions of dense SrTi1-xFexO3-δ (x= 0.25, 0.35, 0.5). J Eur Ceram Soc. 2017;37:2629-36.
[57] Magdeski J. The porosity dependence of mechanical properties of sintered alumina. Journal of the University of Chemical Technology and Metallurgy. 2010;45:143-8.
[58] Aono H, Sugimoto E, Sadaaka Y, Imanaka N, Adachi GJJotES. Ionic conductivity of the lithium titanium phosphate (Li/sub 1+ x/M/sub x/Ti/sub 2-x/(PO/sub 4/)/sub 3/, M= Al, Sc, Y, and La) systems. 1989;136:590.
[59] Withers PJ, Bhadeshia H. Residual stress. Part 2–Nature and origins. Materials science and technology. 2001;17:366-75.

Tables Captions

Table 1. Rietveld refined lattice parameters of as-sintered LATP.

Table 1. Rietveld refined lattice parameters of as-sintered LATP.

	Lattice parameters						
	Space group	*a** (nm)	*b** (nm)	*c** (nm)	α	β	γ
LATP	R-3c h (167)	0.85523	0.85523	2.09652	90°	90°	120°

Figures Captions

Fig. 1. Illustration of relation between the crystal coordinate system and principal sample coordinate system represented by Euler angles [1].

Fig. 2. A schematic of the resolved point load in (a), Schmid factor derivation for a single slip system in (b) and the rotated slip systems in (c).

Fig. 3. Typical SEM image of LATP sample in different magnification.

Fig. 4. XRD pattern of as-sintered LATP sample.

Fig. 5. Nyquist plot of the LATP material at 25 °C.

Fig. 6. The microstructure of LATP material in (a), of which the red and blue marked areas are chosen for indentation test , and (b) the corresponding EBSD result in three axes.

Fig. 7. Typical load-displacement curves for indentation test in specific orientation: (a) on the plane close to basal plane, (b) and (c) on the prismatic type planes.

Fig. 8. Experimentally derived mechanical properties of the LATP as a function of the corresponding angle: (a) elastic modulus and (b) hardness, here the colorful surface map is the guide for the eye to see the dependency of mechanical properties on rotation angle.

Fig. 9. SEM images of the typical imprint morphologies in (a) and (b).

Fig. 10. Indentation elastic modulus and hardness ratio as a function of angle Φ in (a) and (b), respectively. Representative angles $\varphi 2$ of -30°, 0° and 30° are selected to see the limited effect of this angel on the mechanical properties.

Fig. 11. A comparison of the experimental anisotropic indentation modulus and the calculated one according to the Vlassak-Nix model in (a), and the normalized experimental anisotropic hardness and the hardness ratio from easy-slip model in (b).

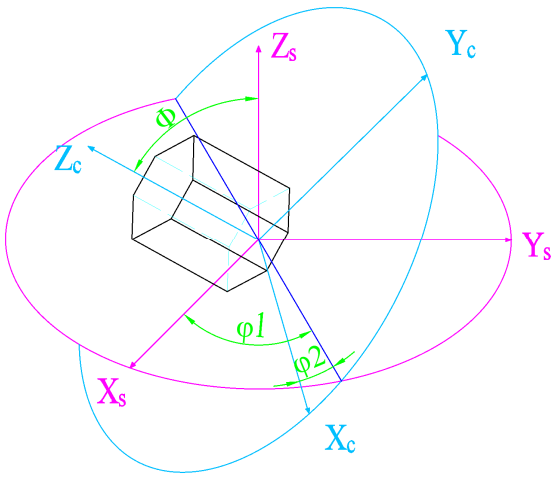

Fig. 1. Illustration of relation between the crystal coordinate system and principal sample coordinate system represented by Euler angles [1].

1. Callister WD, Rethwisch DG (2007) Materials science and engineering: an introduction, vol 7. John Wiley & Sons New York,

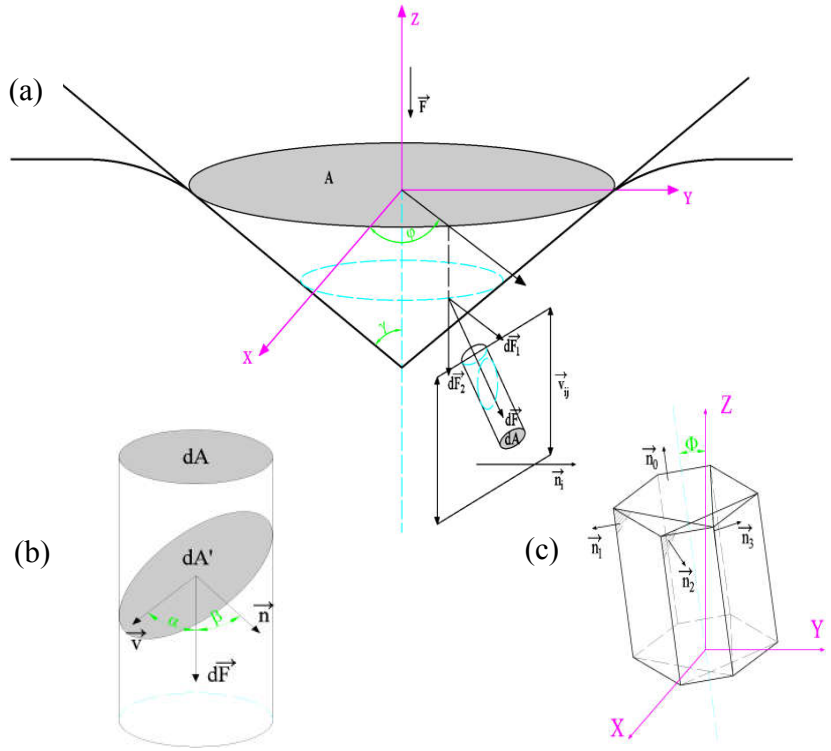

Fig. 2. A schematic of the resolved point load in (a), Schmid factor derivation for a single slip system in (b) and the rotated slip systems in (c).

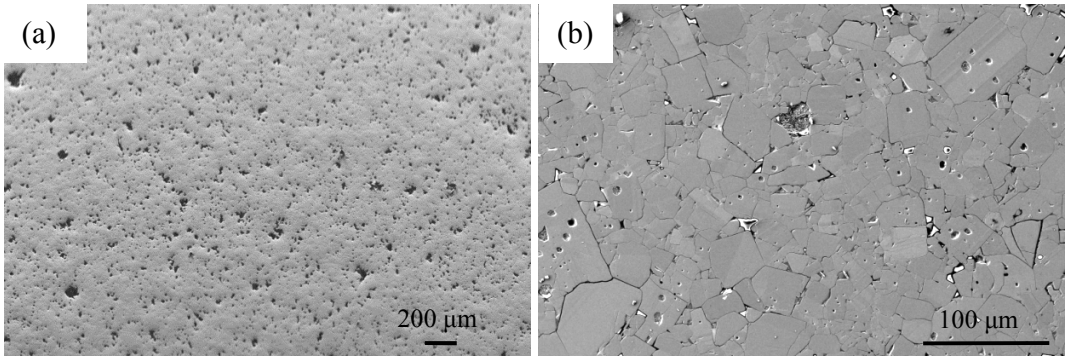

Fig. 3. Typical SEM image of LATP sample in different magnification.

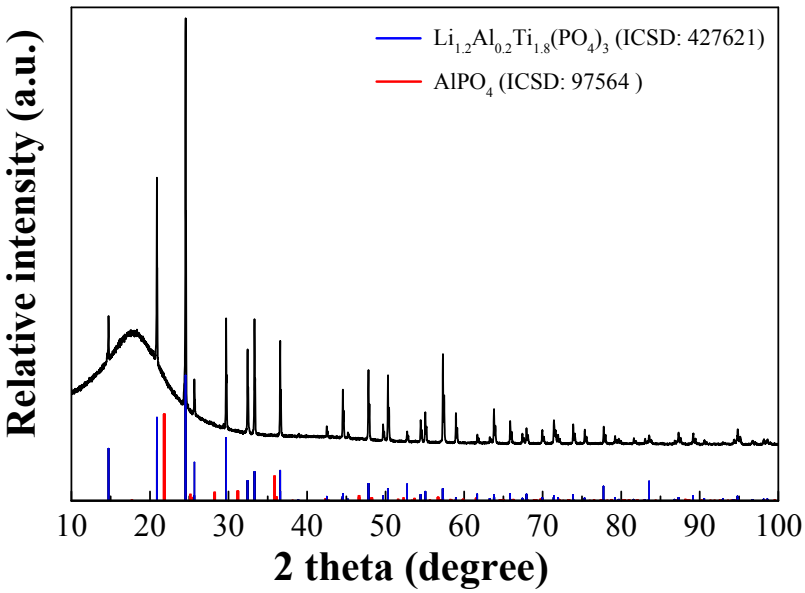

Fig. 4. XRD pattern of as-sintered LATP sample.

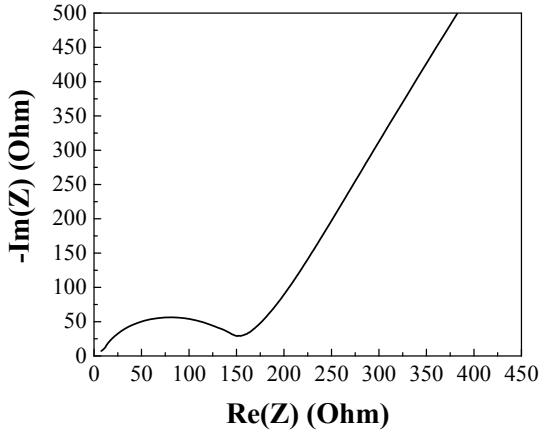

Fig. 5. Nyquist plot of the LATP material at 25 °C.

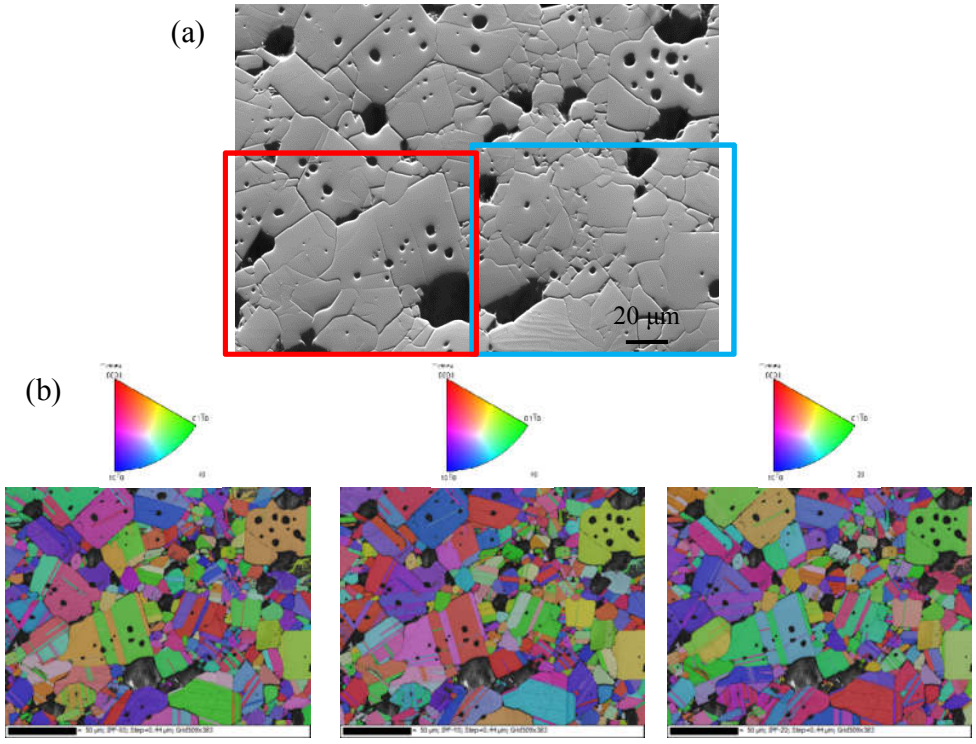

Fig. 6. The microstructure of LATP material in (a), of which the red and blue marked areas are chosen for indentation test , and (b) the corresponding EBSD result in three axes.

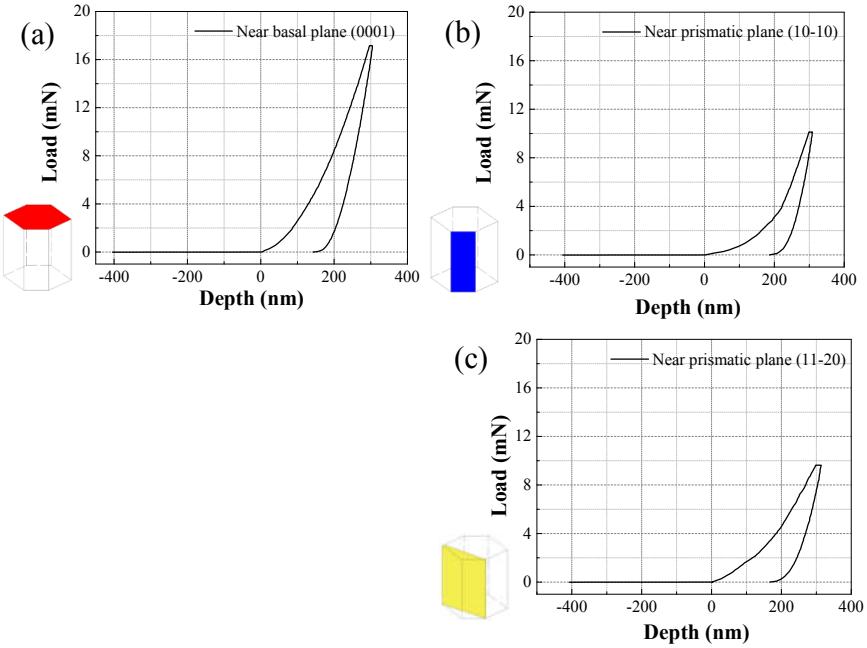

Fig. 7. Typical load-displacement curves for indentation test in specific orientation: (a) on the plane close to basal plane, (b) and (c) on the prismatic type planes.

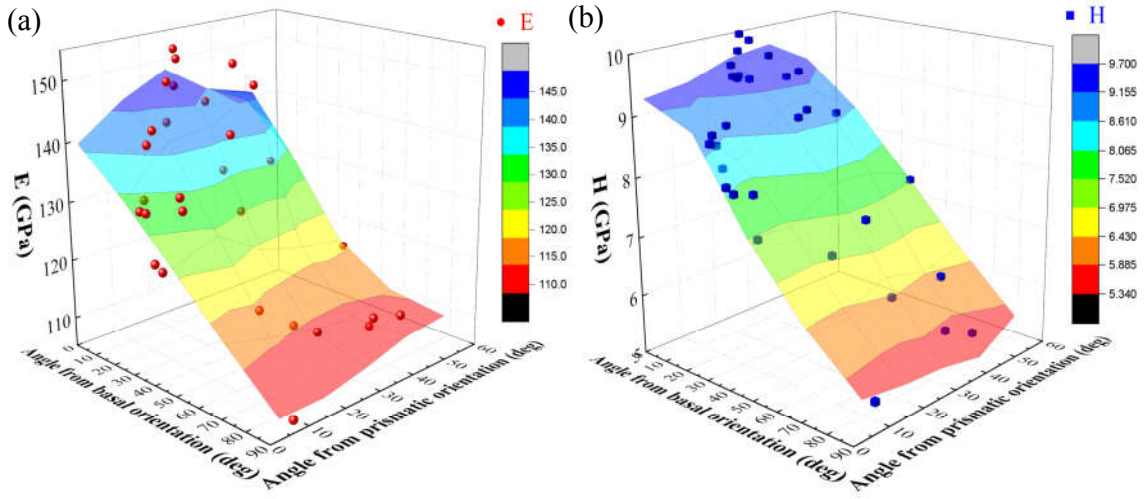

Fig. 8. Experimentally derived mechanical properties of the LATP as a function of the corresponding angle: (a) elastic modulus and (b) hardness, here the colorful surface map is the guide for the eye to see the dependency of mechanical properties on rotation angle.

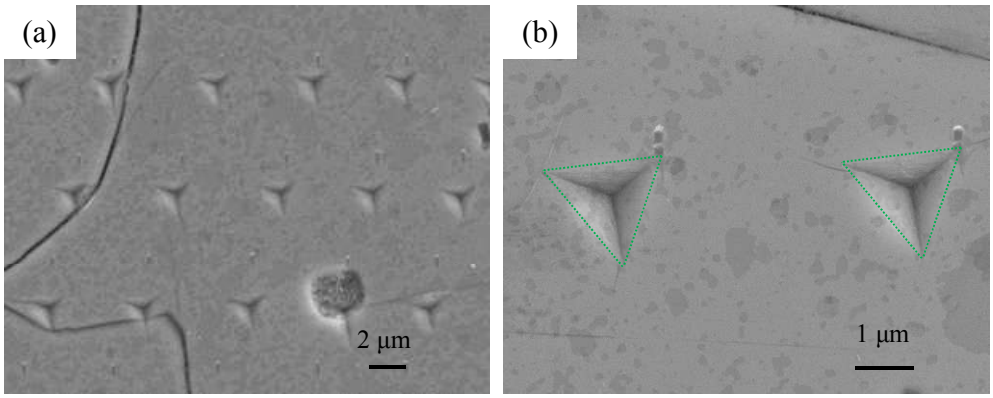

Fig. 9. SEM images of the typical imprint morphologies in (a) and (b).

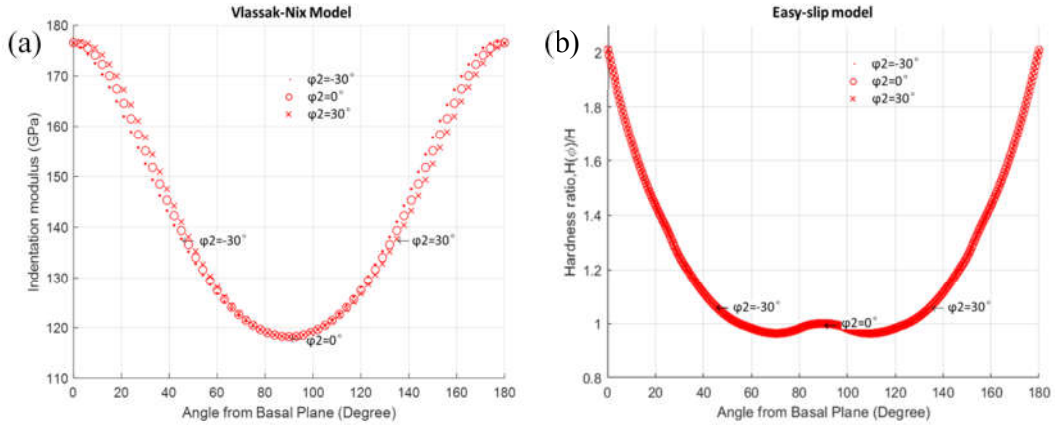

Fig. 10. Indentation elastic modulus and hardness ratio as a function of angle Φ in (a) and (b), respectively. Representative angles $\varphi 2$ of -30°, 0° and 30° are selected to see the limited effect of this angel on the mechanical properties.

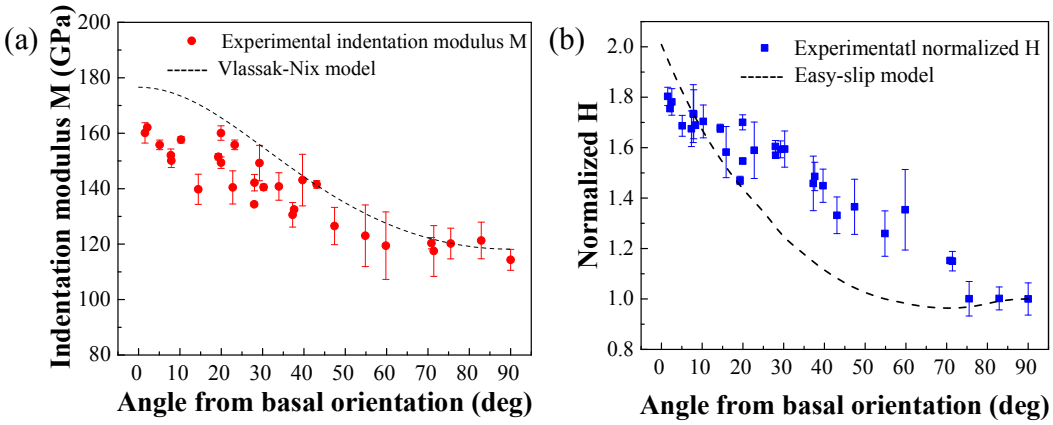

Fig. 11. A comparison of the experimental anisotropic indentation modulus and the calculated one according to the Vlassak-Nix model in (a), and the normalized experimental anisotropic hardness and the hardness ratio from easy-slip model in (b).